
This is an electronic reprint of the original article.
This reprint may differ from the original in pagination and typographic detail.

Benítez, Erika; Méndez-Abreu, Jairo; Fuentes-Carrera, Isaura; Cruz-González, Irene; Martínez, Benoni; López-Martin, Luis; Jiménez-Bailón, Elena; León-Tavares, Jonathan; Chavushyan, Vahram H.

Characterization of a Sample of Intermediate-type AGNs. I. Spectroscopic Properties and Serendipitous Discovery of New Dual AGNs

Published in:
The Astrophysical Journal

DOI:
[10.1088/0004-637X/763/1/36](https://doi.org/10.1088/0004-637X/763/1/36)

Published: 01/01/2013

Document Version
Publisher's PDF, also known as Version of record

Please cite the original version:
Benítez, E., Méndez-Abreu, J., Fuentes-Carrera, I., Cruz-González, I., Martínez, B., López-Martin, L., Jiménez-Bailón, E., León-Tavares, J., & Chavushyan, V. H. (2013). Characterization of a Sample of Intermediate-type AGNs. I. Spectroscopic Properties and Serendipitous Discovery of New Dual AGNs. *The Astrophysical Journal*, 763(1), 13. <https://doi.org/10.1088/0004-637X/763/1/36>

This material is protected by copyright and other intellectual property rights, and duplication or sale of all or part of any of the repository collections is not permitted, except that material may be duplicated by you for your research use or educational purposes in electronic or print form. You must obtain permission for any other use. Electronic or print copies may not be offered, whether for sale or otherwise to anyone who is not an authorised user.

CHARACTERIZATION OF A SAMPLE OF INTERMEDIATE-TYPE AGNs. I. SPECTROSCOPIC PROPERTIES AND SERENDIPITOUS DISCOVERY OF NEW DUAL AGNs

ERIKA BENÍTEZ¹, JAIRO MÉNDEZ-ABREU^{2,3}, ISAURA FUENTES-CARRERA⁴, IRENE CRUZ-GONZÁLEZ¹, BENONI MARTÍNEZ¹,
LUIS LÓPEZ-MARTÍN^{2,3}, ELENA JIMÉNEZ-BAILÓN¹, JONATHAN LEÓN-TAVARES⁵, AND VAHRAM H. CHAVUSHYAN⁶

¹ Instituto de Astronomía, Universidad Nacional Autónoma de México, Apdo. Postal 70-264, México D.F. 04510, Mexico; erika@astro.unam.mx

² Instituto de Astrofísica de Canarias, E-38200 La Laguna, Tenerife, Spain

³ Departamento de Astrofísica, Universidad de La Laguna, E-38205 La Laguna, Tenerife, Spain

⁴ Escuela Superior de Física y Matemáticas, Instituto Politécnico Nacional (ESFM-IPN), U.P. Adolfo López Mateos, México D.F. 07730, Mexico

⁵ Aalto University Metsähovi Radio Observatory, Metsähovintie 114, FI-02540, Kylmälä, Finland

⁶ Instituto Nacional de Astrofísica, Óptica y Electrónica, Apdo. Postal 51-216, 72000 Puebla, Mexico

Received 2011 October 4; accepted 2012 November 26; published 2013 January 3

ABSTRACT

A sample of 10 nearby intermediate-type active galactic nuclei (AGNs) drawn from the Sloan Digital Sky Survey is presented. The aim of this work is to provide estimations of the black hole (BH) mass for the sample galaxies from the dynamics of the broad-line region. For this purpose, a detailed spectroscopic analysis of the objects was done. Using Baldwin–Phillips–Terlevich diagnostic diagrams, we have carefully classified the objects as true intermediate-type AGNs and found that $80\%_{-17.3\%}^{+7.2\%}$ are composite AGNs. The BH mass estimated for the sample is within $6.54 \pm 0.16 < \log M_{\text{BH}} < 7.81 \pm 0.14$. Profile analysis shows that five objects (J120655.63+501737.1, J121607.08+504930.0, J141238.14+391836.5, J143031.18+524225.8, and J162952.88+242638.3) have narrow double-peaked emission lines in both the red ($\text{H}\alpha$, $[\text{N II}] \lambda\lambda 6548, 6583$ and $[\text{S II}] \lambda\lambda 6716, 6731$) and the blue ($\text{H}\beta$ and $[\text{O III}] \lambda\lambda 4959, 5007$) regions of the spectra, with velocity differences (ΔV) between the double peaks within $114 \text{ km s}^{-1} < \Delta V < 256 \text{ km s}^{-1}$. Two of them, J121607.08+504930.0 and J141238.14+391836.5, are candidates for dual AGNs since their double-peaked emission lines are dominated by AGN activity. In searches of dual AGNs, type 1, type II, and intermediate-type AGNs should be carefully separated, due to the high serendipitous number of narrow double-peaked sources ($50\% \pm 14.4\%$) found in our sample.

Key words: galaxies: active – galaxies: nuclei – galaxies: Seyfert

Online-only material: color figures

1. INTRODUCTION

Among nearby active galactic nuclei (AGNs) the so-called Seyfert (Sy) galaxies are commonly found. Seyfert galaxy properties were described in the early work by Khachikian & Weedman (1974) who classified them as Sy 1 and Sy 2 depending on the line widths observed in their optical spectra. A few years later, Osterbrock (1981) introduced different subclasses of Sy galaxies according to the relative intensity showed by the broad emission lines in their spectra. In particular, he introduced the intermediate Sy class, spanning from Sy 1.2 to Sy 1.9. For instance, an Sy 1.8 galaxy shows weak, but readily visible broad $\text{H}\alpha$ and $\text{H}\beta$ emission lines, while an Sy 1.9 shows only a broad $\text{H}\alpha$ component. Recently, Tadhunter (2008) reviewed the general classification and unification of AGNs where Sy 1 and Sy 2 galaxies are more generally grouped as type 1 and type 2 AGNs. Since intermediate-type Sy galaxies do show broad emission-line components, they belong to the type 1 class, but they are more difficult to find since sometimes the intensity of these components can be very low. We will refer to these objects as intermediate-type AGNs to distinguish them from the more general type 1 class.

Early studies on intermediate-type AGNs have proposed that the origin of spectroscopically observed weak emission lines produced in the clouds of the broad-line region (BLR) could be explained by internal reddening (Osterbrock 1981; Goodrich 1990, 1995). Another explanation based in the unified model for AGNs (Urry & Padovani 1995) assumes that a dusty torus located some parsecs away from the central source blocks part

of the emission. Other possibility is that their weak lines could be due to an intrinsically faint non-thermal continuum emission, maybe due to variations in the ionizing continuum (see Trippe et al. 2010 and references therein).

On the other hand, the availability of high-quality spectra of AGNs in the Sloan Digital Sky Survey (SDSS; York et al. 2000) makes it possible to identify intermediate-type AGNs and furthermore study them as a class, in order to find their place in the black hole (BH) demography for nearby AGNs (see Ho 2004). In general, new estimates of fundamental parameters like the BH mass or M_{BH} in AGNs can contribute to the understanding of the associated fueling mechanisms. The M_{BH} can be estimated using different empirically calibrated scaling relations in samples designed to study particular types of AGNs (e.g., Wandel et al. 1999; Vestergaard & Peterson 2006). In particular, BH mass estimates can be obtained using the correlation between the AGN continuum luminosity (Kaspi et al. 2000, 2005) and the BLR radius. By combining continuum luminosity with the width of the $\text{H}\beta$ emission line (in objects that have $z < 1$, otherwise this line goes to the IR), it is possible to estimate the mass of the BH by using a single AGN spectrum, yielding BH masses that are accurate to a factor of ~ 3 (Vestergaard & Peterson 2006).

In the case of intermediate-type AGNs, estimates of the M_{BH} need to be done systematically. Previous works in this type of AGNs are based on single or very few objects (e.g., Osterbrock 1981; Goodrich 1989; Rafanelli et al. 1993; Xanthopoulos 1996; Popović & Mediavilla 1997; Quillen et al. 2000; Torrealba et al. 2006). A larger number of objects was recently studied by Trippe

et al. (2010). These authors selected a sample of 34 previously classified Sy1.8/1.9 and found that 18 are misclassified objects. Therefore, it is necessary to carefully classify candidates in order to establish if they conform to a true sample of intermediate-type AGNs.

Among the type 1 and type 2 AGN samples drawn from the SDSS, the sample of double-peaked narrow emission-line AGNs stands out. Usually they show [O III] line profiles with velocities splitting in the range 151–1314 km s⁻¹. The relevance of studying these kind of AGNs is based on the idea that they are candidates for sub-kpc or kpc-scale dual AGNs (e.g., Comerford et al. 2009). Discovering new dual (or binary, if their nuclei appears separated on pc-scales) AGN candidates is fundamental to constrain models of galaxy formation and evolution. Since it is commonly believed that mergers can trigger or enhance nuclear accretion, it is fundamental to establish their frequency by means of detecting dual or binary AGNs. Nevertheless, it is a fact that direct observational evidence for binary supermassive black holes still remains scarce (see McGurk et al. 2011 and references therein).

Double-peaked [O III] line profiles could arise from several mechanisms (e.g., Xu & Komossa 2009; Rosario et al. 2010; Fu et al. 2011; Shen et al. 2011): (1) the orbital motion of a binary AGN, (2) gas kinematics in extended narrow-line regions (NLRs), and (3) unresolved nuclear gas kinematics (e.g., aligned outflows or disk rotation on small scales). Fu et al. (2012) have obtained high-resolution imaging of 106 narrow double-peaked AGNs (37 type 1 and 69 type II) and found that 31 have companions within 3". Their integral field spectroscopic observations have allowed them to group the narrow double-peaked AGNs in the above three broad categories, according to the origin of the double-peaked [O III] line profiles, finding that only 4.5%–12% are binaries. Other studies on the frequency of these objects among AGNs (e.g., Wang et al. 2009; Liu et al. 2010; Smith et al. 2010) have shown that there are 340 objects between 0.008 < z < 0.686 or, equivalently, ~1% of the entire SDSS AGN sample harboring possible dual AGNs. Nevertheless, the recent study done by Fu et al. (2012) shows that several objects classified in the literature as “binary” are, most likely, single AGNs with extended NLRs. Therefore, the frequency of double-peak objects and binaries among intermediate-type AGNs are still unknown, and so this is worth investigating.

The aim of this work is to isolate intermediate-type AGN objects and estimate their BH mass. In particular, we are interested in providing new estimates that can contribute to the study of the BH demography in nearby AGNs. For this purpose, we present the spectral analysis of a sample of 10 nearby (10⁴² erg s⁻¹ ≲ L_{bol} ≲ 10⁴⁴ erg s⁻¹) intermediate-type AGNs (i.e., intermediate Sy galaxies). Spectral analysis will provide a more precise classification through the use of Baldwin–Phillips–Terlevich (BPT) diagnostic diagrams. A detailed profile decomposition allowed us to discover new narrow double-peaked AGN candidates among the objects in the sample.

The paper is organized as follows. In Section 2 we describe the sample selection and in Section 3 the analysis of the SDSS spectroscopic data. Section 4 shows the results obtained for the sample and relevant properties of some individual objects. The discussion and conclusions are presented in Section 5. An Appendix on the available X-ray data for one of the selected sources is presented. The cosmology adopted for this work is H₀ = 70 km s⁻¹ Mpc⁻¹, Ω_m = 0.3, and Ω_λ = 0.7.

Table 1
Intermediate-type AGN Sample

Galaxy No.	SDSS ID	Other Name	z	D _L (Mpc)	M _g
1	J120655.63+501737.1	SBS 1204+505B	0.062	278.01	16.20
2	J121600.04+124114.3	Mrk 764	0.066	296.78	14.87
3	J121607.08+504930.0	Mrk 1469	0.031	135.92	15.27
4	J141238.14+391836.5	NGC 5515	0.026	113.58	13.78
5	J143031.18+524225.8	SBS 1428+529	0.044	194.77	15.25
6	J144049.35+505009.2	SBS 1439+510	0.117	544.65	17.28
7	J153810.05+573613.1	SBS 1537+577	0.073	329.87	15.51
8	J162952.88+242638.3	Mrk 883	0.038	167.47	15.26
9	J212851.19–010412.4	IC 1385	0.052	231.51	15.21
10	J234428.81+134946.0	...	0.068	306.21	16.32

Notes. Column 1: galaxy identification. Column 2: SDSS id. Column 3: other names. Column 4: redshift by NED. Column 5: luminosity distance. Column 6: Petrosian g-band magnitude given in SDSS-DR7.

2. SAMPLE SELECTION

We selected objects flagged as quasars (QSO) in the SDSS database that have Petrosian g-band magnitudes between 14 ≲ m_g ≲ 17 and redshifts within 0.026 < z < 0.12, i.e., a sample of nearby AGNs. From this sample, we chose only those galaxies that have spectroscopic data in the SDSS database in order to accurately obtain their spectral classification. An additional condition imposed was that visually all selected galaxies should have spectral characteristics of intermediate-type AGNs. We ended up with a sample of 23 candidates that were photometrically observed with the Nordic Optical Telescope. Results obtained with these data are presented in a companion paper (Benítez et al. 2012, hereafter Paper II). A final sample of 10 candidates for intermediate-type AGNs were chosen for this work, these are presented in Table 1. The remaining objects were taken out from the sample since after a preliminary analysis of their spectra, we found that some of them were either narrow-line Seyfert 1 (Osterbrock & Pogge 1985) or Seyfert 1 objects.

3. ANALYSIS OF SDSS-DR7 SPECTRA

The optical SDSS-DR7 spectra of our sample were processed using the STARLIGHT code (Cid Fernandes et al. 2005; Mateus et al. 2006). This code has been successfully used to study some AGN samples (see Bian et al. 2007; Stasińska et al. 2006; Rafanelli et al. 2009; Cid Fernandes et al. 2011; Coziol et al. 2011; Mezcuca et al. 2011; León-Tavares et al. 2011). In a first run, all spectra were corrected for Galactic extinction using the dust maps of Schlegel et al. (1998) and the extinction law of Cardelli et al. (1989). Also in this first run, in order to obtain the signal-to-noise ratio (S/N) we have masked the most prominent emission lines that are known to be present in the composite spectra of QSOs (see Francis et al. 1991). So, the following lines were masked: [O II] λλ3726, 3729, [Ne III] λ3869, He I λ3970, Hδ λ4102, Hγ λ4340, Hβ λ4861, [O III] λ λ4959, 5007, He I λ5876, [O I] λ6300, Hα λ6562, [N II] λλ6548, 6583, and [S II] λλ6717, 6731; together with the interstellar medium absorption from Na D λ5890 Å). The S/N was obtained for each spectrum in the wavelength range of 4730–4780 Å and is presented in Column 2 of Table 2.

Based on the S/N previously obtained, each spectrum was randomly perturbed 100 times using a Monte Carlo seed. Our lowest S/N value was 5.9, so the perturbations varied ±16% of

Table 2
Optical Spectroscopic Parameters

Galaxy No.	S/N	FWHM (H α) (km s $^{-1}$)	FWHM (H β) (km s $^{-1}$)	log [O III]/H β			log [N II]/H α			log [S II]/H α		
				blue	red	single-peak	blue	red	single-peak	blue	red	single-peak
1	13.5 \pm 0.4	2950 \pm 58	2565 \pm 284	0.96 \pm 0.06	0.20 \pm 0.01		-0.31 \pm 0.02	-0.17 \pm 0.10		-0.54 \pm 0.03	-0.57 \pm 0.03	
2	9.2 \pm 0.2	4860 \pm 158	5549 \pm 449*			0.18 \pm 0.01			-0.34 \pm 0.02			-1.14 \pm 0.05
3	8.8 \pm 0.2	6700 \pm 69	6190 \pm 739	1.06 \pm 0.04	1.24 \pm 0.05		-0.13 \pm 0.01	0.19 \pm 0.01		-0.41 \pm 0.02	0.23 \pm 0.01	
4	8.3 \pm 0.2	3551 \pm 279	4068 \pm 489*	0.35 \pm 0.01	0.34 \pm 0.01		-0.06 \pm 0.002	-0.07 \pm 0.002		-0.34 \pm 0.01	-0.38 \pm 0.01	
5	5.9 \pm 0.1	3878 \pm 341	4438 \pm 583*	0.12 \pm 0.01	0.37 \pm 0.02		-0.19 \pm 0.01	-0.13 \pm 0.01		-0.53 \pm 0.02	-0.52 \pm 0.02	
6	6.5 \pm 0.4	3194 \pm 143	2584 \pm 519			0.32 \pm 0.04			-0.15 \pm 0.02			-0.51 \pm 0.06
7	10.6 \pm 0.3	2491 \pm 38	2788 \pm 187			0.16 \pm 0.01			-0.34 \pm 0.02			-0.64 \pm 0.04
8	11.5 \pm 0.3	2776 \pm 87	3187 \pm 219*	0.76 \pm 0.04	0.18 \pm 0.01		-0.29 \pm 0.02	-0.35 \pm 0.02		-0.12 \pm 0.01	-0.48 \pm 0.02	
9	10.7 \pm 0.4	1955 \pm 25	2443 \pm 101			0.42 \pm 0.03			-0.24 \pm 0.02			-0.66 \pm 0.05
10	6.3 \pm 0.5	2094 \pm 38	2442 \pm 178			0.52 \pm 0.10			-0.36 \pm 0.07			-0.70 \pm 0.13

Notes. Column 1: galaxy no. (cf. Table 1). Column 2: SDSS spectra S/N obtained from STARLIGHT (Cid Fernandes et al. 2005). Column 3: FWHM(H α) broad component. Column 4: FWHM(H β) broad component. Columns 5–7: log [O III]/H β line ratios for double-peaked objects (blue and red) and for single-peaked sources. Columns 8–10: log [N II]/H α line ratios for double-peaked objects (blue and red) and for single-peaked sources. Columns 11–13: log [S II]/H α line ratios for double and single-peaked sources. Note that we mark objects with an * where the FWHM(H β) was obtained using Shen et al. (2008); see the text.

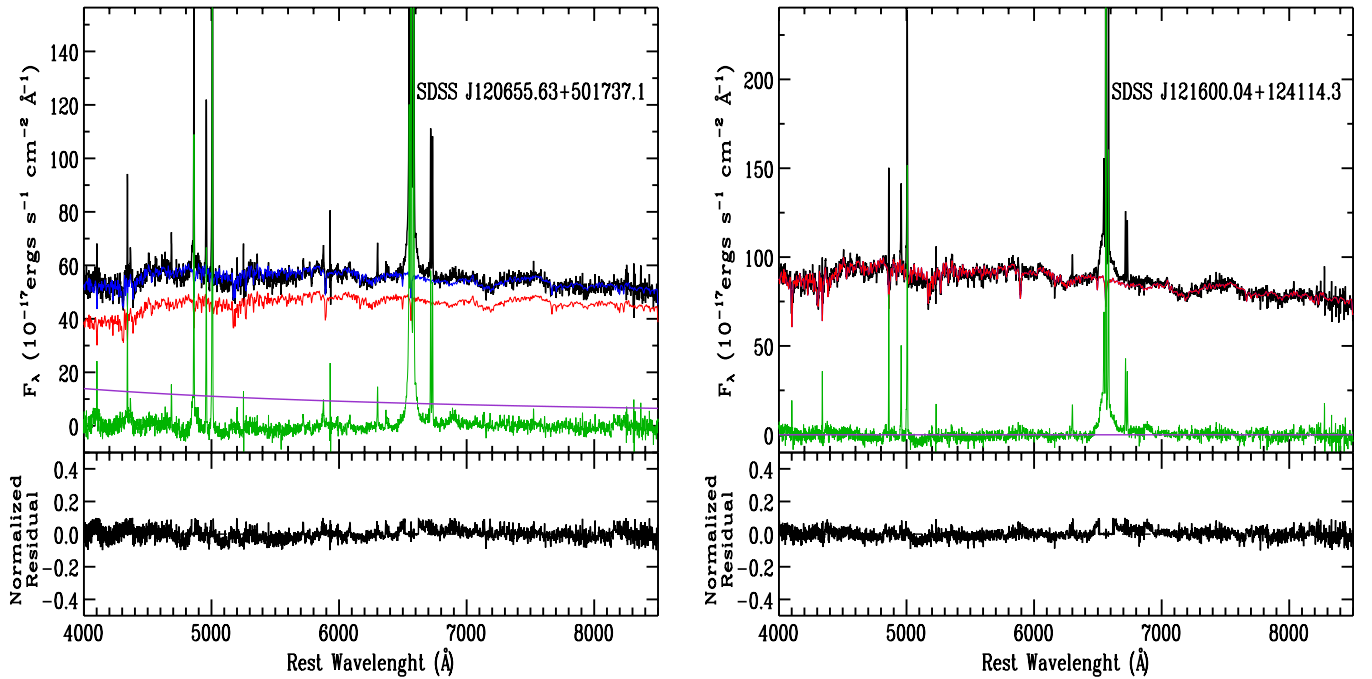


Figure 1. STARLIGHT fit of the SDSS spectra. The black line shows the original SDSS de-redshifted spectrum. The red line shows the pure stellar continuum spectrum and the purple line the power law used to fit the AGN continuum. The blue line shows the best fit to the data and represents the sum of the red spectrum plus the AGN continuum. We show in green the final pure AGN spectra of J120655.63+501737.1 and J121600.04+1241143. Bottom panels show the normalized residuals. (A color version of this figure is available in the online journal.)

the signal value. We obtained 100 simulated spectra per object that were also analyzed with STARLIGHT, masking again the prominent emission lines as we did in the first run. From these simulated spectra, we obtained a collection of 100 models for the absorption spectrum of the host galaxy, from which we will obtain an estimation of the velocity dispersion. We chose the median of the distribution of models as our best model of the host-galaxy absorption spectrum. The stellar velocity dispersion σ_* was estimated from the median value of the distribution and the quoted errors are the rms values (see Table 5). In all cases the obtained σ_* is larger than 65 km s^{-1} , which is the nominal SDSS velocity resolution (e.g., Liu et al. 2010). The AGN continuum flux at 5100 \AA was estimated from the collection of 100 power-law fittings. Again we chose the best fit from the median value of the distribution of models to obtain $F_{5100 \text{ \AA}}$ and the rms as the associated error. This flux will be used to derive the BH mass, as is described in Section 4.1. Therefore, STARLIGHT provided us with the best synthetic spectra for our AGN sample.

The original SDSS spectra and the final pure AGN spectra, together with the obtained fits for the sample objects are shown in Figures 1–5. These figures show how the stellar contribution is subtracted with STARLIGHT from the composite spectra. This is essential for our study since the absorption synthetic spectra were used to estimate the velocity dispersion and the pure AGN spectra to perform a line profile analysis. An example of the best model obtained for object 9 is shown in Figure 6, where it can be seen how STARLIGHT is capable of fitting the absorption lines used to estimate the velocity dispersion along with the stellar continuum. The absorption lines used to estimate σ_* are marked in the blow-up spectrum.

The complete optical spectroscopic parameters obtained for the sample are presented in Table 2. The FWHM for both the $H\alpha$ and $H\beta$ broad components have errors $<10\%$. The line ratios have also errors $<10\%$ except for object 10, which

has errors $\sim 18\%$. The profile decomposition in all cases was done using the algorithm PeakFit.⁷ From our profile decomposition analysis, we find that in five objects (objects 1, 3, 4, 5, and 8) the $[\text{O III}] \lambda\lambda 4959, 5007$, $[\text{S II}] \lambda\lambda 6716, 6731$, $[\text{N II}] \lambda\lambda 6548, 6583$ doublets and the narrow components of $H\alpha$ and $H\beta$ clearly show a double-peaked profile. The spectral profile decomposition of these five narrow-double peaked AGNs are shown in Figures 7–11. We have checked the redshifts using some absorption lines from the host-galaxy spectra and found that they are in good agreement with the values reported in NED⁸, which are based mainly on emission lines. Therefore, the Gaussians centroids were forced to correspond to the host-galaxy redshift. For all objects, the widths of the Gaussians fitted to the narrow lines have the same Doppler broadening, and the intensity ratio $[\text{O III}] \lambda 5007 / [\text{O III}] \lambda 4959$ was fixed to its theoretical value. Table 3 presents the velocity difference defined as $\Delta V = V_{\text{red}} - V_{\text{blue}}$ for each object with double-peaked narrow emission lines for various lines.

Baldwin et al. (1981) propose a suite of diagnostic diagrams (known as BPT) to classify emission-line galaxies in order to disentangle the dominant energy source. The diagrams are based on four optical line ratios: $[\text{O III}]/H\beta$, $[\text{N II}]/H\alpha$, $[\text{S II}]/H\alpha$, and $[\text{O I}]/H\alpha$. Following Kewley et al. (2006), we present in Figure 12 two BPT diagnostic diagrams that show the location of the sample objects. These diagrams used line ratios $[\text{O III}]/H\beta$, $[\text{N II}]/H\alpha$, and $[\text{S II}]/H\alpha$.

We note that for the narrow double-peaked objects we present the obtained line ratios separately using the blue and red components. This allowed us to see how objects can change their spectral classification in the diagnostic diagram. We have

⁷ Systat Software Inc. <http://www.sigmaplot.com>.

⁸ The NASA/IPAC Extragalactic Database (NED) is operated by the Jet Propulsion Laboratory, California Institute of Technology, under contract with the National Aeronautics and Space Administration.

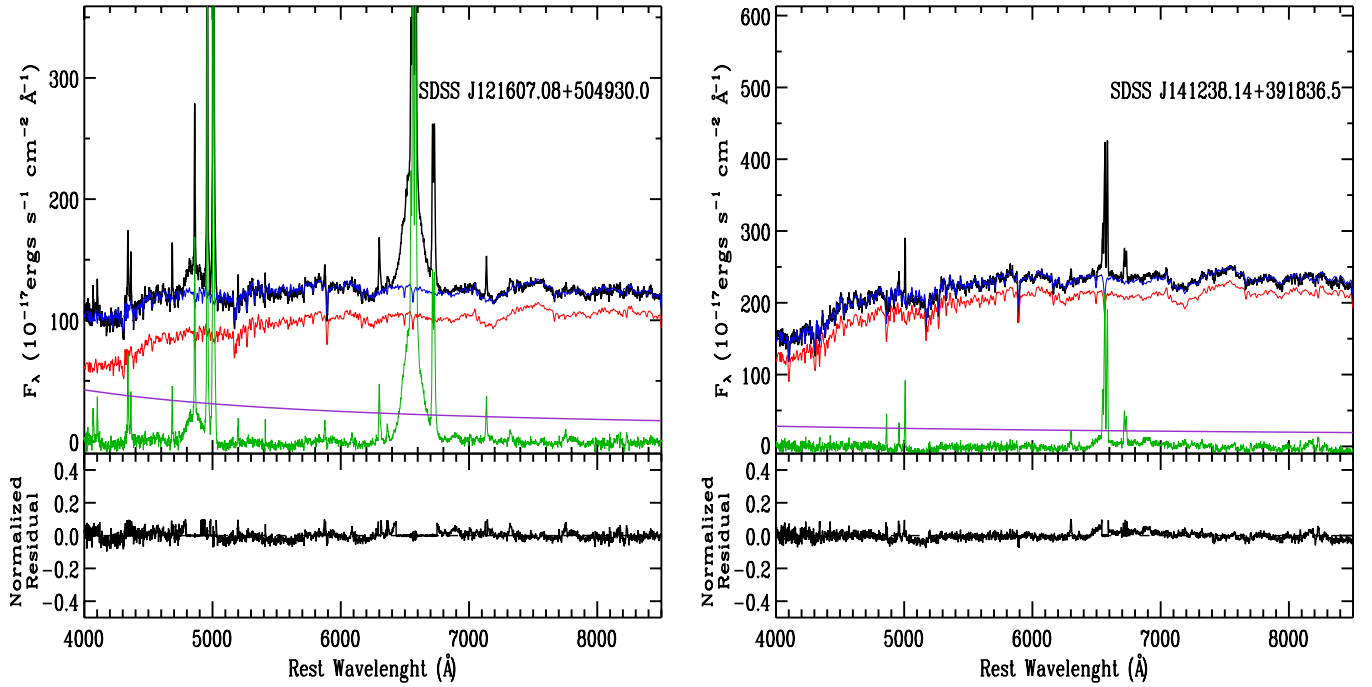


Figure 2. Spectra of J121607.08+504930.0 and J141238.14+391836.5. Same as Figure 1.

(A color version of this figure is available in the online journal.)

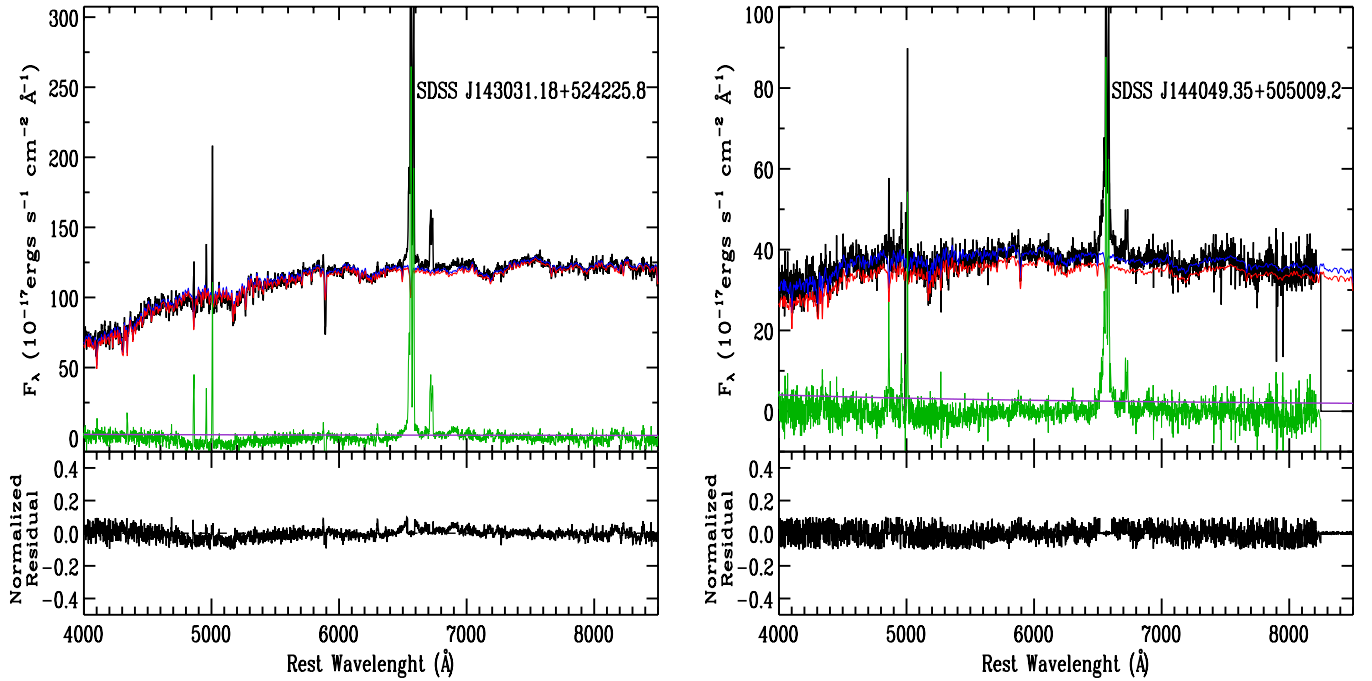


Figure 3. Spectra of J143031.18+524225.8 and J144049.35+505009.2. Same as Figure 1.

(A color version of this figure is available in the online journal.)

found that eight objects are composite AGNs (starburst plus AGNs). In Table 5, we present the spectral classification obtained for all objects. In some objects, we obtained different classifications since they appear in different places in the two BPT diagrams. In particular, object 2 appears as a starburst (SB) galaxy in one of the BPT diagrams. In addition, since all objects present a broad-line component, and following Whittle (1992), we have obtained their Sy type based on $F_{5007}/F_{H\beta} = R$. Then, we have assigned Sy 1 ($R \leq 0.3$),

Sy 2 ($0.3 < R \leq 1$), Sy 1.5 ($1 < R \leq 4$), Sy 1.8 ($R > 4$), and Sy 1.9 if only broad $H\alpha$ was seen.

4. RESULTS

4.1. M_{BH} Estimates

The M_{BH} for all objects in the sample were indirectly derived using an empirically calibrated photoionization method (Wandel et al. 1999; Vestergaard 2002; Vestergaard & Peterson

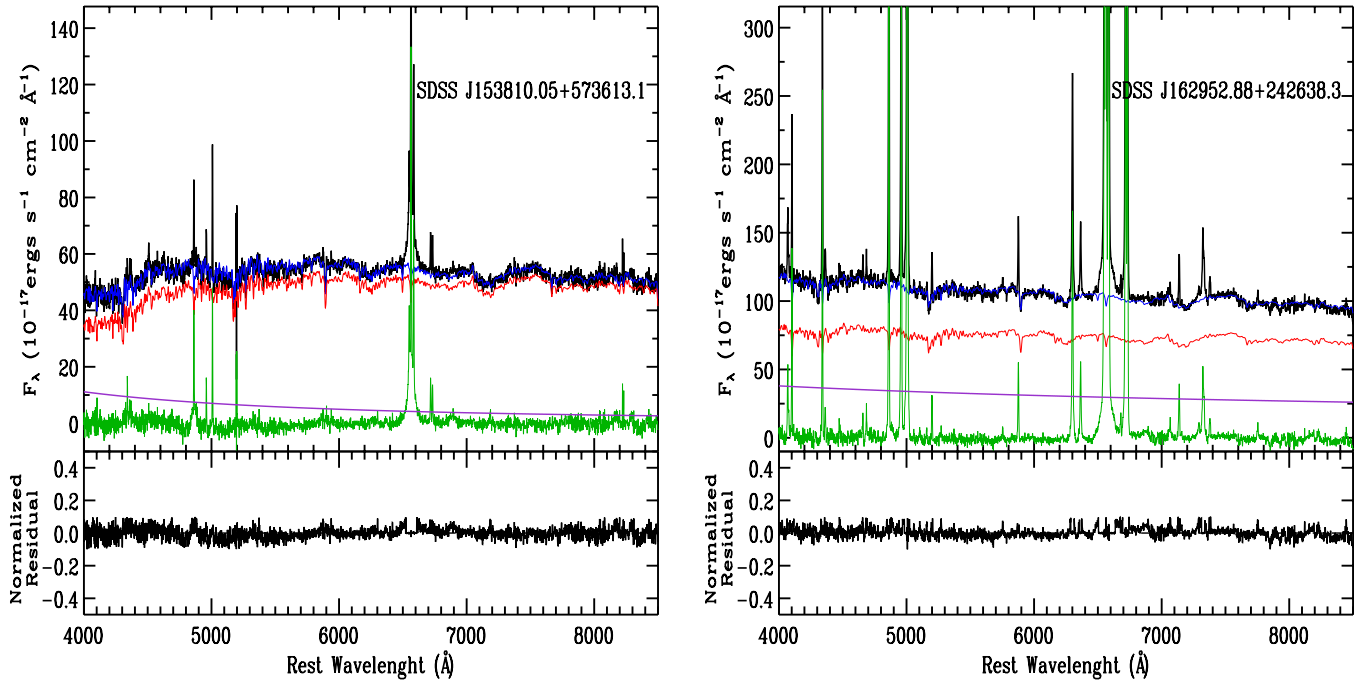


Figure 4. Spectra of J153810.05+573613.1 and J162952.88+242638.3. Same as Figure 1.
(A color version of this figure is available in the online journal.)

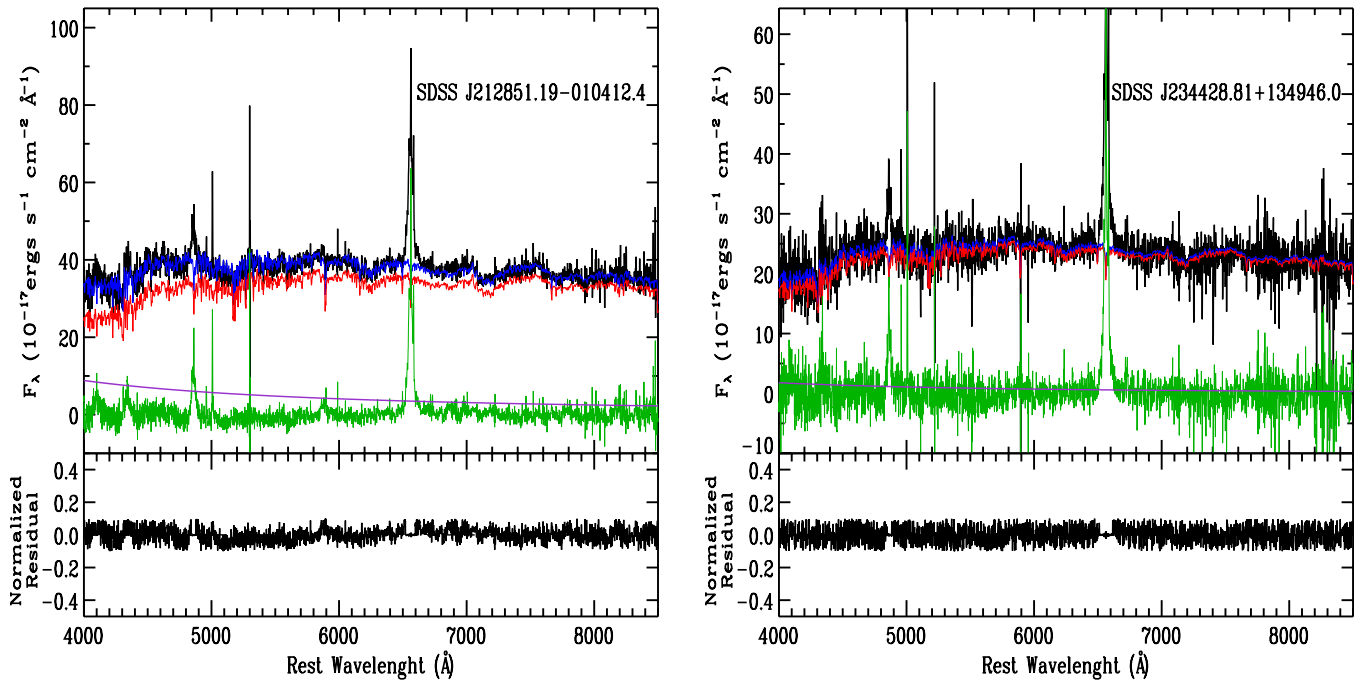


Figure 5. Spectra of J212851.19-010412.4 and J234428.81+134946.0. Same as Figure 1.
(A color version of this figure is available in the online journal.)

2006). We derived BH masses from the SDSS-DR7 spectra using Equation (5) from Vestergaard & Peterson (2006), which makes use of the FWHM of the H β emission line and the continuum luminosity at 5100 Å. Luminosity at 5100 Å (L_{5100}) was estimated from the median flux derived with the power-law fit done with STARLIGHT and the luminosity distances of the objects using the redshifts given in NED. The bolometric luminosity was obtained using $L_{\text{bol}} \sim 9\lambda L_{\lambda 5100}$ (see Kaspi et al. 2000), which yields the Eddington ratio $L_{\text{bol}}/L_{\text{Edd}}$, where

$L_{\text{Edd}} \approx 1.3 \times 10^{38} (M_{\text{BH}}/M_{\odot})$. Our luminosity results are shown in Table 4. For objects without the H β broad component, the H α line FWHM was converted to H β FWHM using Equation (3) in Shen et al. (2008). The BH mass estimates for our sample are shown in Table 5.

We can also derive the BH mass using the so called $M-\sigma_*$ relation (Ferrarese & Merritt 2000; Gebhardt et al. 2000) and see if these estimates are in agreement with the BH mass derived for these objects using scaling relations. This is the reason why

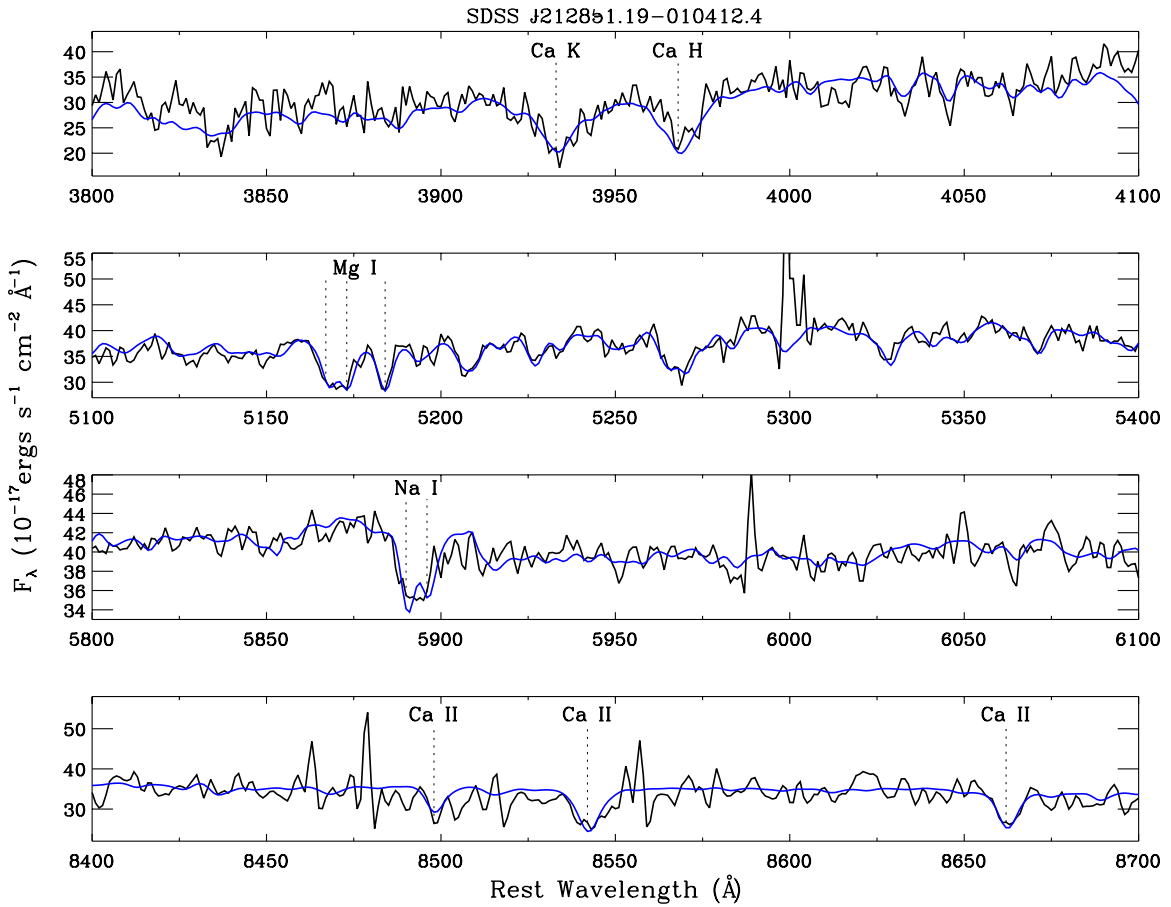


Figure 6. Blow-up of our best model obtained from Monte Carlo simulations for the spectrum of J212851.19–010412.4. This fit is shown also in blue in the left panel of Figure 5. The lines used to estimate the velocity dispersion are marked with vertical dotted lines.

(A color version of this figure is available in the online journal.)

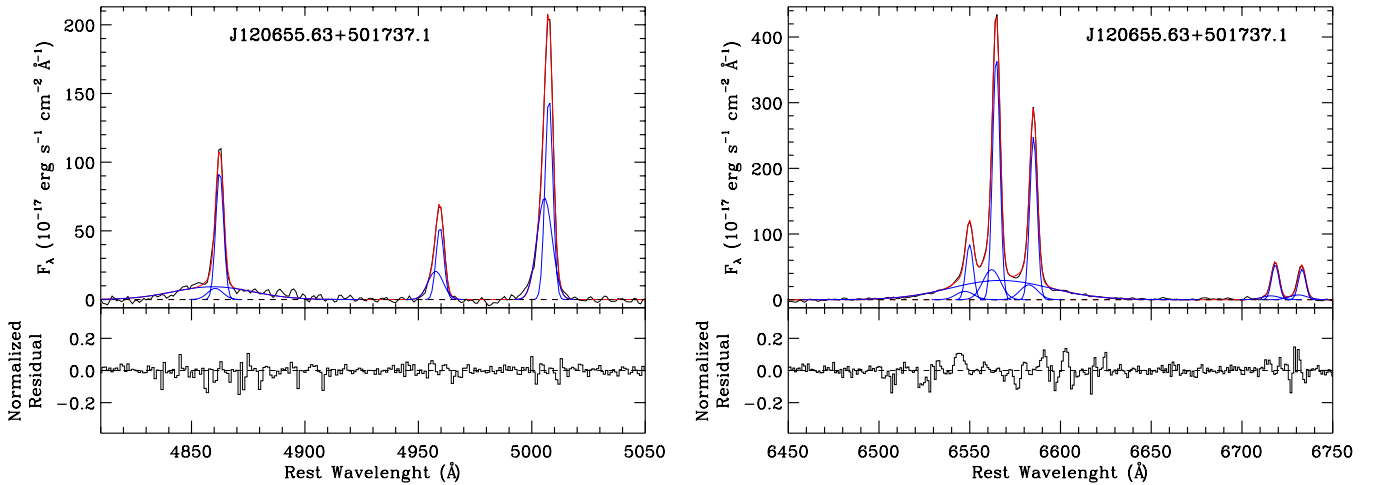


Figure 7. Spectral decomposition for SDSS J120655.63+501737.1. Left and right panels show our best fit obtained for the blue and red part of the spectrum, respectively. In both panels, black lines correspond to the pure AGN spectrum obtained with STARLIGHT; blue lines show the Gaussian components used for the fit and red lines the best fit obtained. At the bottom of each panel the corresponding normalized residuals are shown. The [O III] λ 4959, 5007 lines and the narrow component of H β were best fitted using two Gaussian components. For the broad component of H β only one Gaussian was needed for the fit. The red part of the spectrum was modeled in a similar way, i.e., two Gaussian components for the narrow lines and one Gaussian for the broad component of H α .

(A color version of this figure is available in the online journal.)

we obtained the velocity dispersion (σ_*) with STARLIGHT. However, since the use of this relation depends on the bulge type associated with the host galaxy (e.g., Hu 2008), we will present these estimates in Paper II, along with a detailed discussion of

the bulge type present in each galaxy based on the photometric and spectroscopic observations.

In Figure 13, we show the BH mass versus luminosity relation obtained for the objects in our sample. The diagonal lines show

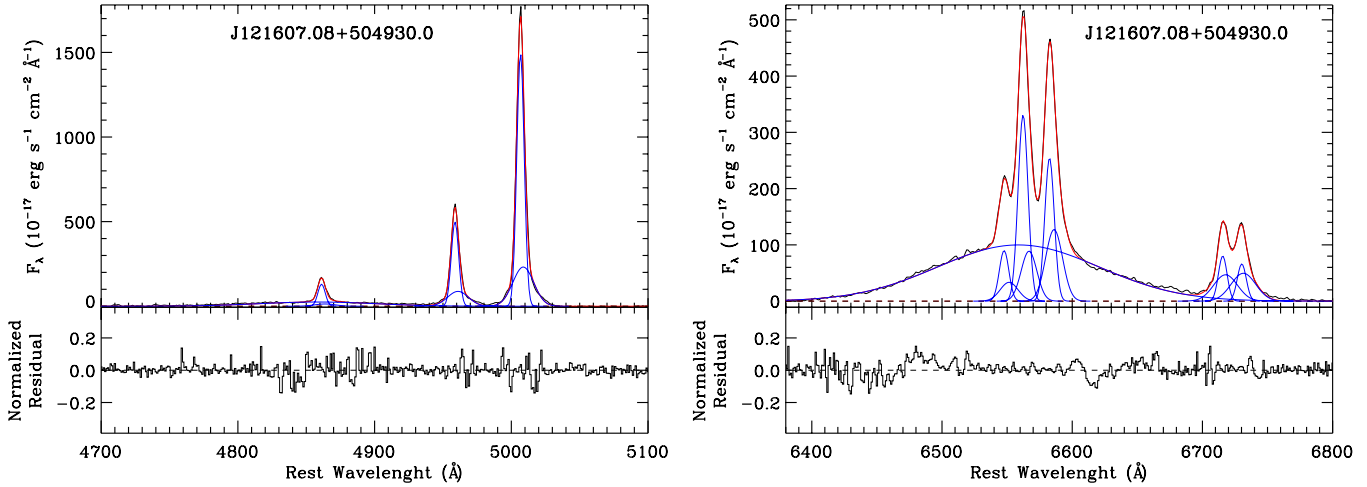


Figure 8. Spectral decomposition for SDSS J121607.08+504930.0. We have modeled the lines in a similar way as described in Figure 7. (A color version of this figure is available in the online journal.)

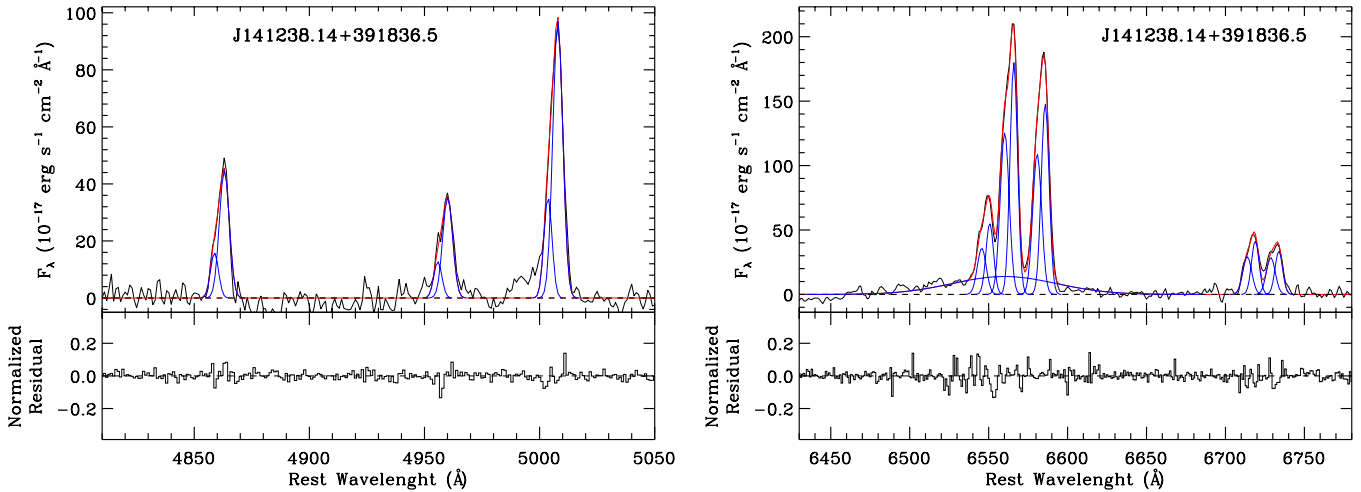


Figure 9. Spectral decomposition for SDSS J141238.14+391836.5. This object has also been modeled using two Gaussian components for the narrow lines. However, when fitting the broad components we found no evidence for a broad component in H β . For the red part of the spectrum a broad Gaussian component was needed to properly fit the H α line, and two Gaussian components for the narrow lines. (A color version of this figure is available in the online journal.)

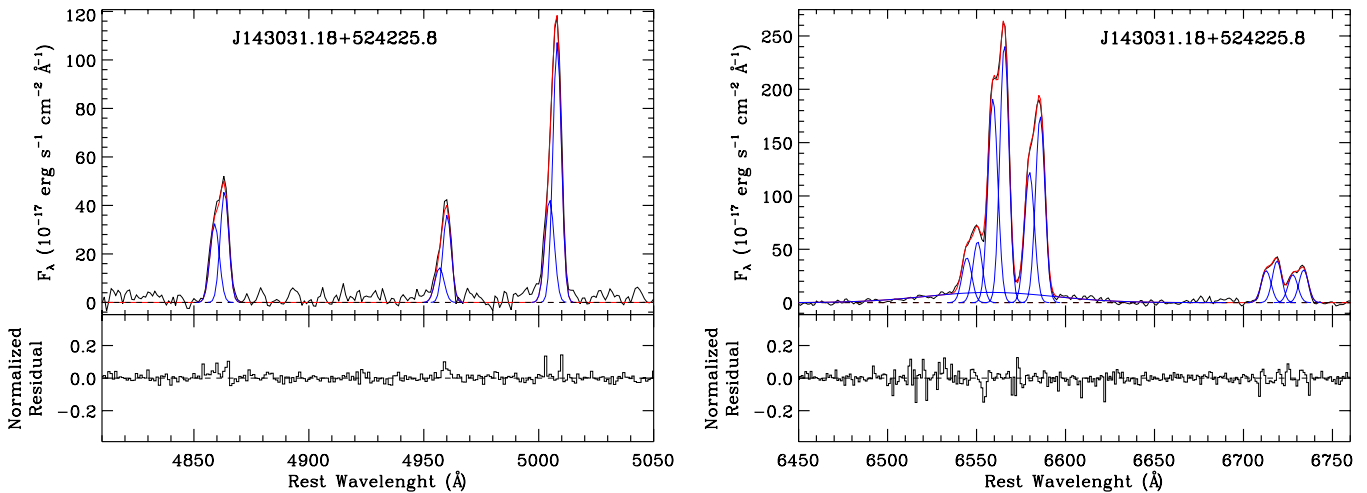


Figure 10. Spectral decomposition for SDSS J143031.18+524225.8. This object has been modeled similar to the one shown in Figure 9. (A color version of this figure is available in the online journal.)

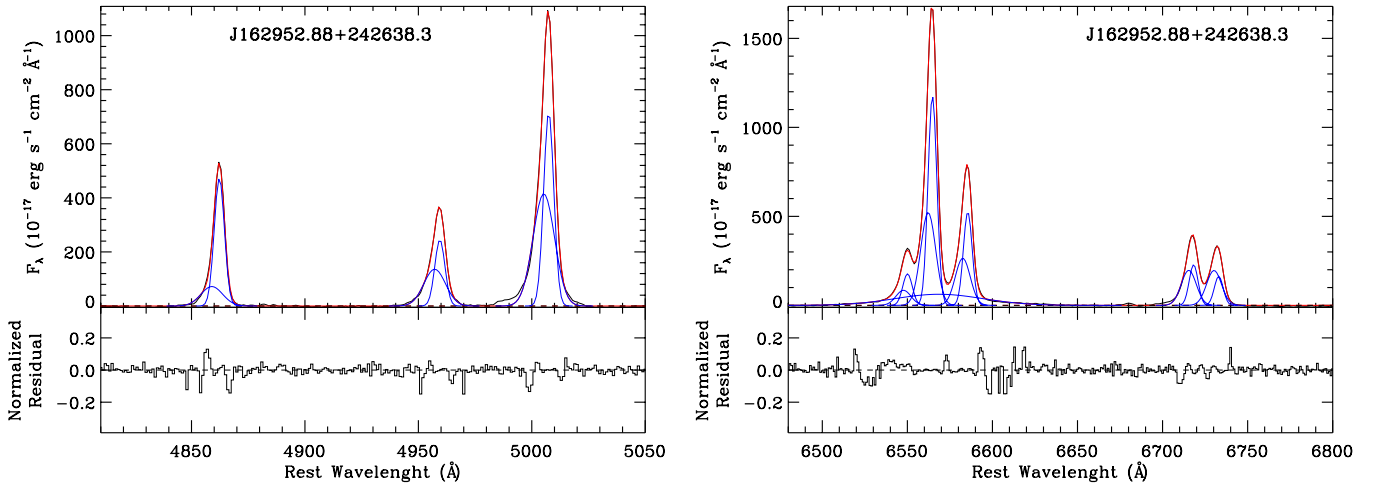


Figure 11. Spectral decomposition for SDSS J162952.88+242638.3. The lines were fitted using three Gaussian components for [O III] λ 4959, 5007 since it shows a wing component in addition to the two narrow components. The red part of the spectrum was fitted using two Gaussian components for the narrow lines. There is no broad component in H β , but a broad component was fitted for H α .

(A color version of this figure is available in the online journal.)

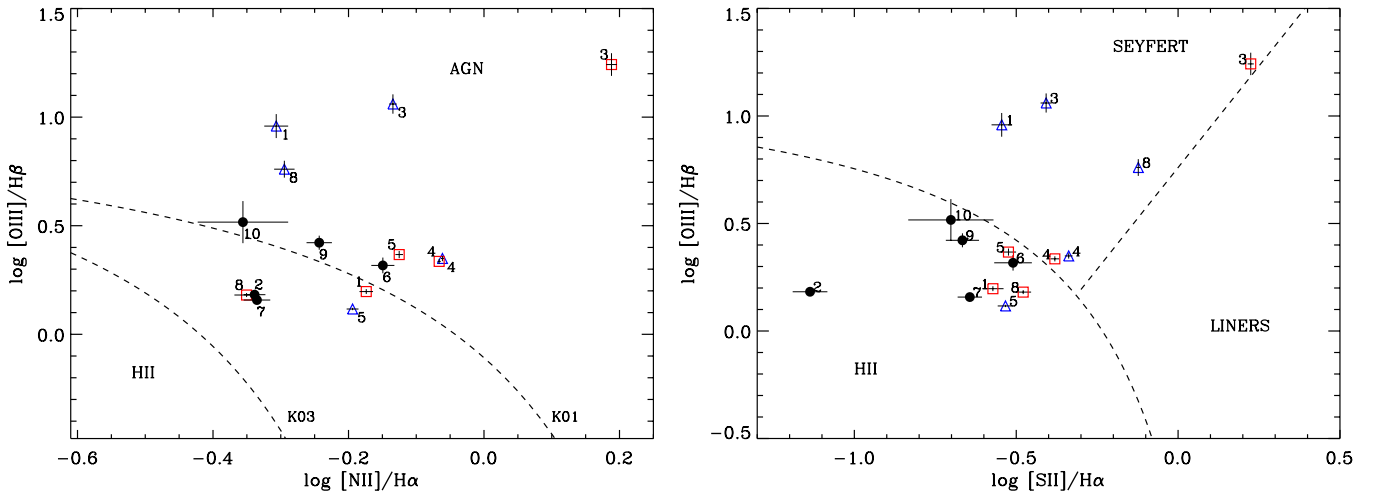


Figure 12. Location of the objects of the sample in two BPT diagnostic diagrams. Left side: the dashed lines come from Kewley et al. (2001, K01) and Kauffmann et al. (2003, K03). Some objects are composite AGNs, i.e., they lie between K01 and K03 lines, meaning that they have a starburst (SB) galaxy plus an AGN. Filled black dots mark the locus of single-peaked objects. Objects with narrow double-peaked emission lines are shown twice since we used the ratios obtained from their red (open squares) and blue (open triangles) components. Right side: BPT diagram showing that all objects are located above the LINER region accordingly with Kewley et al. (2006). The spectral classification is presented in Table 5.

(A color version of this figure is available in the online journal.)

Table 3
Velocity Differences in Narrow Double-peaked AGNs

SDSS	J120655.63+501737.1	J121607.08+504930.0	J141238.14+391836.5	J143031.18+524225.8	J162952.88+242638.3
	(No. 1)	(No. 3)	(No. 4)	(No. 5)	(No. 8)
Line	ΔV (km s $^{-1}$)				
H α λ 6562.74	116 \pm 17	209 \pm 122	264 \pm 15	296 \pm 5	115 \pm 3
[N II] λ 6548	117 \pm 31	177 \pm 48	232 \pm 28	276 \pm 32	110 \pm 17
[N II] λ 6583	118 \pm 5	160 \pm 107	231 \pm 32	274 \pm 12	135 \pm 5
[S II] λ 6716	111 \pm 15	97 \pm 9	226 \pm 7	272 \pm 15	128 \pm 7
[S II] λ 6731	96 \pm 35	56 \pm 8	226 \pm 13	271 \pm 20	123 \pm 7
H β λ 4861.29	120 \pm 11	160 \pm 10	263 \pm 80	264 \pm 17	142 \pm 20
[O III] λ 4959	118 \pm 35	132 \pm 26	258 \pm 18	199 \pm 185	139 \pm 10
[O III] λ 5007	116 \pm 11	120 \pm 7	256 \pm 120	198 \pm 64	130 \pm 3
Average value	114 \pm 7	139 \pm 45	245 \pm 16	256 \pm 34	128 \pm 11

Notes. Velocity differences obtained between the red and the blue Gaussian components ($\Delta V = V_{\text{red}} - V_{\text{blue}}$). Column 1: line rest frame. Columns 2–6: velocity differences obtained for SDSS objects J120655.63+501737.1, J121607.08+504930.0, J141238.14+391836.5, J143031.18+524225.8, and J162952.88+242638.3, respectively. Last row indicates the average ΔV value and standard deviation of each object considering all lines.

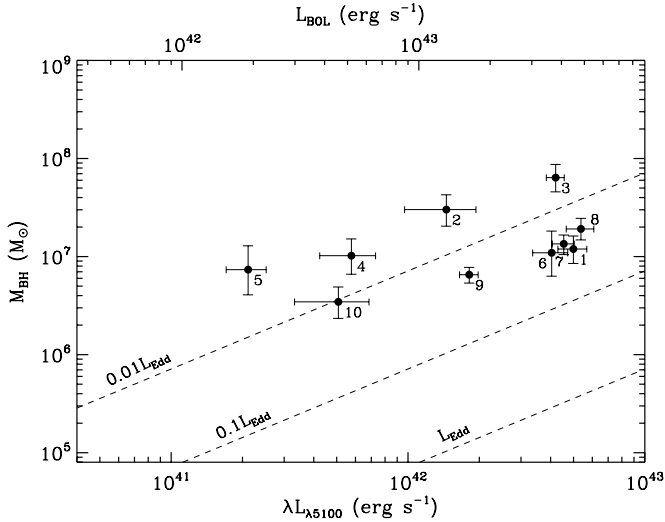


Figure 13. Diagram of M_{BH} vs. luminosity. The upper x -axis shows the bolometric luminosity assuming $L_{\text{bol}} \sim 9\lambda L_{\lambda 5100}$.

Table 4
Luminosities and Eddington Rates

Galaxy No.	$\lambda L_{\lambda 5100}$ (10^{41} erg s $^{-1}$)	L_{bol} (10^{42} erg s $^{-1}$)	L_{Edd} (10^{44} erg s $^{-1}$)	$L_{\text{bol}}/L_{\text{Edd}}$ (10^{-2})
1	49.92 ± 6.98	45 ± 6.28	15.05 ± 5.08	2.98 ± 1.42
2	14.52 ± 4.84	13.07 ± 4.36	37.99 ± 14.24	3.44 ± 0.24
3	42.02 ± 3.65	37.82 ± 3.28	80.45 ± 26.41	0.47 ± 0.20
4	5.77 ± 1.53	5.19 ± 1.38	12.87 ± 5.39	0.40 ± 0.28
5	2.11 ± 0.41	1.90 ± 0.37	9.27 ± 5.38	0.21 ± 0.16
6	40.43 ± 6.83	36.39 ± 6.14	13.77 ± 7.32	2.64 ± 0.02
7	45.47 ± 4.90	40.92 ± 4.37	16.98 ± 3.96	2.41 ± 0.82
8	53.74 ± 7.17	48.37 ± 6.45	24.12 ± 6.03	2.01 ± 0.01
9	18.14 ± 1.63	16.33 ± 1.47	8.23 ± 1.43	1.98 ± 0.52
10	5.08 ± 1.76	4.57 ± 1.59	4.35 ± 1.59	1.11 ± 0.75

Notes. Column 1: galaxy no. (cf. Table 1). Column 2: luminosity at 5100 Å measured using a continuum power-law fit. Column 3: bolometric luminosities obtained assuming $L_{\text{bol}} = 9\lambda L_{\lambda 5100}$. Column 4: Eddington luminosities using our estimated M_{BH} . Column 5: Eddington ratio.

the Eddington limits shown by our objects. Note that internal extinction has not been taken into account. All objects have low to moderate accretion Eddington rates ($L_{\text{bol}}/L_{\text{Edd}} < 0.11$).

4.2. Double-peaked Objects

Spectral analysis showed that among our objects we have five objects that clearly show narrow double-peaked emission lines: galaxies 1, 3, 4, 5, and 8 (cf. Table 1). In Table 3 we present the velocity differences, $\Delta V = V_{\text{red}} - V_{\text{blue}}$, for H α , [N II] $\lambda 6583$, [N II] $\lambda 6583$, [S II] $\lambda 6716$, [S II] $\lambda 6731$, H β , [O III] $\lambda 4959$, and [O III] $\lambda 5007$ lines. Our definition of a narrow-line double-peaked object requires that in all these lines a double-peaked Gaussian component should be present. The average values and standard deviation obtained for each source are listed in the bottom line of this table, which shows that they are within $114 \text{ km s}^{-1} \lesssim \Delta V \lesssim 256 \text{ km s}^{-1}$.

4.3. Notes on Particular Objects

4.3.1. J120655.63+501737.1 (Object 1)

The profile decomposition shows that this AGN was best fitted using double-peaked lines for its NLR (see Figure 7). Its

Table 5
BH Mass

Galaxy No.	σ_* (km s $^{-1}$)	$\log M_{\text{BH}}$ (M_{\odot})	Spectral Classification	Double-peak
1	90 ± 6	7.08 ± 0.14	Sy 1.8 + SB/Sy 1.5 + SB	Yes
2	111 ± 6	7.48 ± 0.16	Sy 1.9 + SB/SB	No
3	147 ± 7	7.81 ± 0.14	Sy 1.8	Yes*
4	195 ± 8	7.01 ± 0.18	Sy 1.9	Yes*
5	165 ± 9	6.86 ± 0.25	Sy 1.5 + SB	Yes
6	188 ± 17	7.04 ± 0.23	Sy 1.5 + SB	No
7	91 ± 6	7.13 ± 0.10	Sy 1.5 + SB	No
8	187 ± 9	7.28 ± 0.11	Sy 1.9 + SB	Yes
9	79 ± 6	6.82 ± 0.08	Sy 1.5 + SB	No
10	93 ± 11	6.54 ± 0.16	Sy 1.8 + SB	No

Notes. Column 1: galaxy no. (cf. Table 1). Column 2: velocity dispersion obtained with STARLIGHT. Errors were estimated from our Monte Carlo simulation on the data; see the text. Column 3: black hole mass estimates were obtained with the relation given by Vestergaard & Peterson (2006). Black hole mass for object 8 have to be taken with care since the host galaxy is probably a merger. Column 4: Sy type. Column 5: yes if it is double peak, and * shows the two dual AGN candidates found in our study.

spectrum was fitted with a broad component for the H β and H α lines, and from its locus in the BPT diagrams shown in Figure 12, we classify this object as a composite AGN. The blue component indicates that it is an Sy 1.8+SB, and the red component that it is an Sy 1.5 + SB.

4.3.2. J121600.04+124114.3 (Object 2)

In Véron-Cetty & Véron (2010) and in NED this object is classified as an Sy 1.9, and in Mazzarella & Balzano (1986) it is classified as an SB galaxy. We agree with both classifications since this object appears in one diagram as a composite Sy 1.9 + SB, and in the other as a clear SB galaxy; cf. Figure 12. We noted that the emission-line fitting of this object clearly needed a double-peaked Gaussian component for [O III], [S II], and [N II] lines, but when fitting the narrow components of H α and H β only one Gaussian component was required. Since we did not need double-peaked Gaussians to fit the narrow-line components of H α and H β , this object was not classified as double-peaked.

4.3.3. J121607.08+504930.0 (Object 3)

The profile decomposition analysis shows that this object is a narrow-line double-peaked AGN; see Figure 8. Its spectrum was fitted with a broad component for the H β and H α lines, and from the locus of each component in the BPT diagnostic diagrams shown in Figure 12, we classify this object as an Sy 1.8 galaxy.

4.3.4. J141238.14+391836.5 (Object 4)

From our profile decomposition, we find that this AGN is a narrow-line double-peaked (Figure 9) source. In addition, we noted that this object lacks a broad component in the H β region. From its locus in the BPT diagrams in Figure 12, and using the blue and the red components, we classify this object as an Sy 1.9 galaxy.

4.3.5. J143031.18+524225.8 (Object 5)

This object is also a narrow-line double-peaked source; see Figure 10. Since we need a broad Gaussian component to fit the H α region and from the BPT diagnostic diagrams in Figure 12,

using both the blue and red components we classify this object as an Sy 1.5 + SB.

4.3.6. J162952.88+242638.3 (Object 8)

The [O III] $\lambda\lambda 4949, 5007$ doublets clearly show a double-peaked profile and a rather broad wing. We fitted the profile with two sets of three Gaussians. Two Gaussian profiles were used for fitting the narrow component of H β (Figure 11). The profile decomposition shows a broad Gaussian component for H α . The BPT diagnostic diagrams in Figure 12 clearly show that, using both red and blue components, the object is a composite AGN and we classify it as an Sy 1.9 + SB. The results on the spectral analysis of the *XMM-Newton* data on this source (see the Appendix) are in agreement with the optical data ones. This is based on the obtained value of the Γ index and the low values found for the equivalent N_{H} . Both values are compatible with type I objects (e.g., Piconcelli et al. 2005).

5. DISCUSSION AND CONCLUSIONS

The sample presented in this work consists of 10 nearby intermediate-type AGNs, some of them showing a weak broad H α line component. An example of this was presented in the profile analysis of J162952.88+242638.3. It clearly shows a rather weak broad component in H α (cf. Figure 11), typical of an Sy 1.9 galaxy. This result is also supported with our analysis of publicly available *XMM-Newton* data on this object that showed that the power index and the hydrogen column absorption are compatible with type 1 (cf. the Appendix) objects. Thus, our Sy 1.9 classification for this object resulted in a disagreement with Trippe et al. (2010), who recently classified this object as an Sy 2 using the same optical and *XMM-Newton* data.

The BPT diagnostic diagram [O III]/H β versus [S II]/H α clearly shows that all single-peaked objects are composite AGNs. In the case of the narrow-line double-peaked objects detected in this work, three are composite AGNs (objects 1, 5, and 8) and only two of them (objects 3 and 4) are pure intermediate Sy galaxies. Therefore, $80\%^{+7.2\%}_{-17.3\%}$ of our intermediate-type objects are composite AGNs. It is interesting to note that using the Whittle (1992) classification for intermediate Sy galaxies, we confirm that all objects studied in this work are intermediate-type AGNs.

The FWHM of the H β component was used to estimate the BH mass in all objects for the first time. We found that the sample studied in this work has a BH mass range of $6.54 \pm 0.16 < \log M_{\text{BH}} < 7.81 \pm 0.14$. In particular three objects (objects 5, 9, and 10) have $M_{\text{BH}} \sim 10^6 M_{\odot}$. Recently, Kormendy et al. (2011) suggested that small BHs in bulgeless galaxies or pseudobulges grow as low-level Sy. This idea will be explored in our companion Paper II, where we study the bulge properties of this sample. Also, in Paper II the M_{BH} estimates obtained in this work will be compared with estimates for the same sample through the use of the $M-\sigma_*$ correlation. We also found that objects in our sample have low to moderate accretion rates that go from $(0.21 \pm 0.23) \times 10^{-2}$ to $(3.44 \pm 0.24) \times 10^{-2}$ and are located at the low tail of bolometric AGN luminosities.

Among the intermediate-type AGNs identified in this sample, $50\% \pm 14.4\%$ show narrow double-peaked emission lines. From the BPT diagrams and following Comerford et al. (2009) we find that two objects, 3 and 4, are good candidates for dual AGNs since both the blue and red emission-line components are dominated exclusively by AGN activity. The other three narrow double-peaked objects 1, 5, and 8 show one emission-line component in the AGN region while the other appears

in the composite AGN + SB region. Therefore, the precise classification of each component in the case of double-peaked AGNs is essential, since it gives hints on the origin of the observed narrow double-peaked lines. This information could be useful in identifying new dual AGNs.

The objects showing narrow double-peaked emission lines found in this work need to be studied through observations enabling spatially resolved imaging and spatially resolved spectroscopy. In searches of dual AGNs, type 1, type 2, and intermediate-type AGNs should be carefully separated due to the serendipitously high number of narrow double-peaked sources found in our sample. These objects could be useful for establishing the properties and origin of narrow double-peaked emission-line profile in cases where the peak velocity separation lies below 300 km s^{-1} .

We thank the anonymous referee for useful suggestions and constructive criticism. We also thank Dr. D. Clark who carefully read the final version of the manuscript. E.B. and B.M. acknowledge financial support from UNAM-DGAPA-PAPIIT through grant IN116211. J.M.A. is partially funded by the Spanish MICINN under the Consolider-Ingenio 2010 Program grant CSD2006-00070 and also by the grants AYA2007-67965-C03-01 and AYA2010-21887-C04-04. I.F.C. thanks the financial support from CONACYT grant 0133520 and IPN-SIP grant 20121700. Funding for the Sloan Digital Sky Survey (SDSS) and SDSS-II has been provided by the Alfred P. Sloan Foundation, the Participating Institutions, the National Science Foundation, the U.S. Department of Energy, the National Aeronautics and Space Administration, the Japanese Monbukagakusho, and the Max Planck Society, and the Higher Education Funding Council for England. The SDSS Web site is <http://www.sdss.org/>. This research has made use of the NASA/IPAC Extragalactic Database (NED) which is operated by the Jet Propulsion Laboratory, California Institute of Technology, under contract with the National Aeronautics and Space Administration.

APPENDIX

XMM-NEWTON DATA ANALYSIS OF J162952.88+242638.3 (OBJECT 8)

We searched for X-ray data available for our sample objects in *Chandra* and *XMM-Newton* databases. We found that only one of our objects has been observed with *XMM-Newton*. This object is J162952.88+242638.3, also known as Mrk 883. The three *XMM-Newton* observations analyzed for this object were performed during 2006 August 13, 15, and 21 (ObsID: 0302260101, 0302260701, and 0302261001, respectively). The exposure times after flare removal (see below) were 7.9, 10.5, and 10.5 ks. All observations were processed using the standard Science Analysis System, SAS v10.3.0 (Gabriel et al. 2004) and using the most updated calibration files available in 2011 January. The EPIC-pn events were filtered due to high background events using the method described in Piconcelli et al. (2004). No signs of pile-up or out-of-time events were detected in any of the observations.

The spectra of each observation were extracted from circles centered in the maximum emission pixel and with radii which maximized the S/N, i.e., $22''/5$. The background circular regions used for the spectral analysis were located close to the source and free of any contaminating source. Both response matrices were generated for each observation using the *arfgen* and

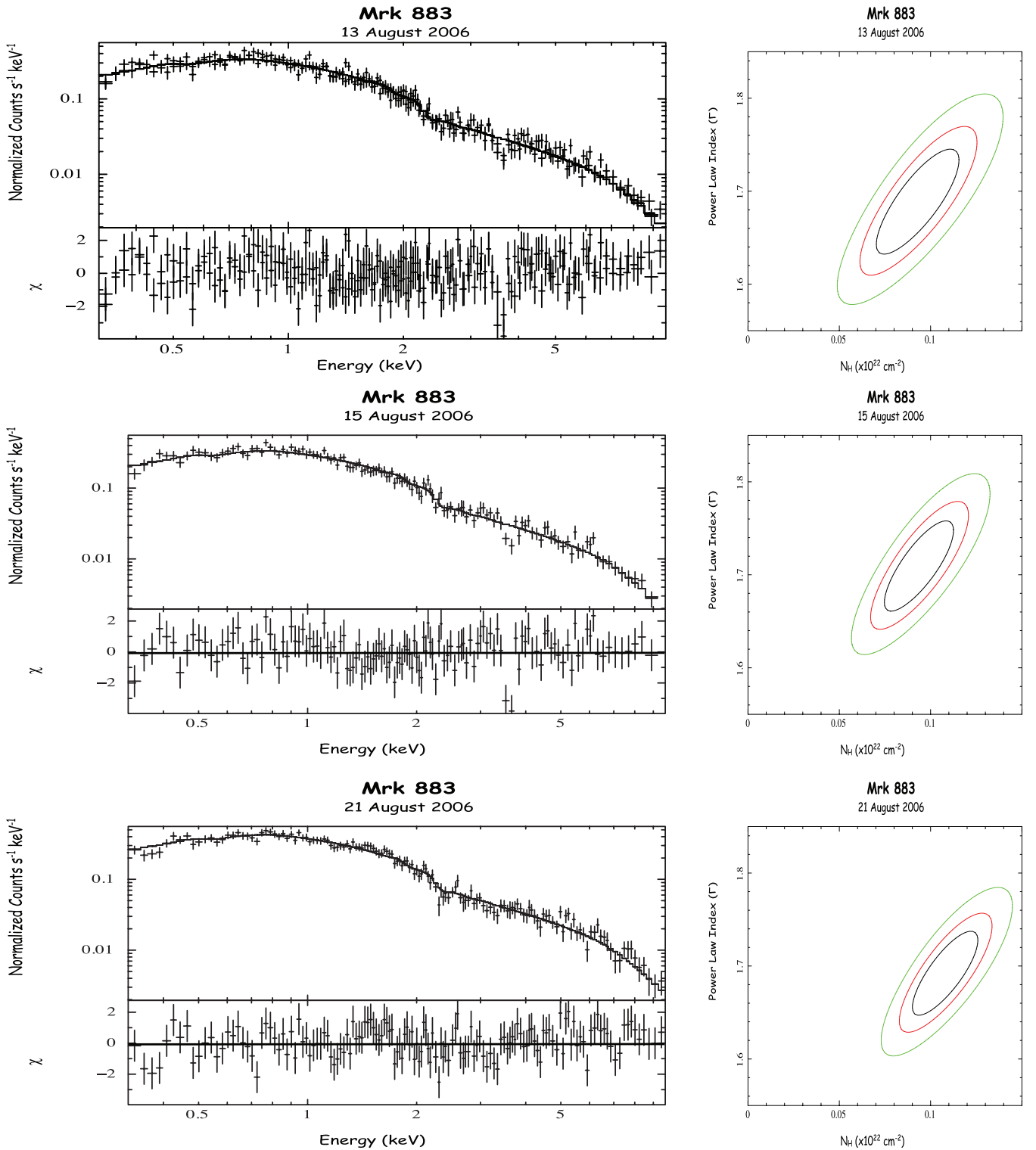


Figure 14. Left column: EPIC-pn observed spectra of SDSS J162952.88+242638.3 (Mrk 883) together with the best-fit model and the residuals. More details of the model can be found in Table 6. Right column: contour plots of the index of the power law and the equivalent hydrogen column density for the three *XMM-Newton* observations of this object. Each line corresponds to a different observation date.

(A color version of this figure is available in the online journal.)

remgen SAS (<http://xmm.esac.esa.int/sas/>) tasks. The spectra were binned to have at least 20 counts per bin in order to be able to use the modified χ^2_{ν} technique (Lampton et al. 1976) for the data fit. All the three spectra were analyzed simultaneously. The shape of the continuum is quite similar among the three observations, with a slight increment of the emission for the third

observation. After taking into account the absorption due to our Galaxy, $N_{\text{H}} = 3.83 \times 10^{20} \text{ cm}^{-2}$, the continuum emission can be satisfactorily fitted with a single absorbed power law with a photon index $\Gamma = 1.7 \pm 0.03$ and an equivalent hydrogen column density of the order of $1 \times 10^{21} \text{ cm}^{-2}$. Table 6 summarizes the values of the parameters for the best-fit model.

Table 6
X-Ray Spectroscopic Parameters

Obs.	Neutral Abs	Power Law	Emission Line		Goodness			Flux		Luminosity		
			Day	Model	N_{H}	Γ	Energy	EW	χ^2_{ν}	dof	F -test	0.5–2 keV
13	A	9 ± 2	1.68 ± 0.06			134.0	118		0.65 ^{+0.03} _{-0.04}	1.51 ± 0.05	2.64 ^{+0.12} _{-0.16}	4.90 ± 0.16
	B	9 ± 2	1.69 ± 0.06	6.4f	<170	133.9	117	35.2%				
	C	10 ± 2	1.70 ± 0.06	6.88 ^{+0.08} _{-0.15}	210 ⁺¹⁸⁰ ₋₁₆₀	129.0	116	87.5%				
15	A	9 ± 2	1.71 ± 0.05			135.0	129		0.66 ± 0.02	1.47 ± 0.05	2.66 ± 0.08	4.79 ± 0.16
	B	10 ± 2	1.72 ± 0.05	6.4f	210 ⁺⁹⁰ ₋₁₅₀	128.9	128	98.5%				
	C	10 ± 2	1.72 ± 0.05	6.34 ^{+0.08} _{-0.10}	200 ⁺¹³⁰ ₋₁₂₀	127.3	127	97.6%				
21	A	11 ± 2	1.69 ± 0.05			128.9	145		0.83 ± 0.03	1.95 ± 0.05	3.43 ± 0.12	6.33 ± 0.16
	B	11 ± 2	1.70 ± 0.05	6.4f	75 ⁺⁴ ₋₃	126.9	144	86.6%				
	C	11 ± 2	1.70 ± 0.05	6.55 ± 0.15	150 ± 110	123.9	143	94.1%				

Notes. Column 1: day of observations, data are from 2006 August. Column 2: model A: absorbed power law; model B: absorbed power law plus a neutral iron line with the energy fixed to 6.4 keV and an iron line with the energy left free to vary were tested. During the eight days which the observations span, moderate flux variability between the first two observations and the last one was detected. Neither power-law index nor intrinsic absorption variation was measured. Figure 14 summarizes the results for the X-ray analysis of SDSS J162953.88+242638.3: the best-fit model for the three spectra with the residuals to the data, and the contour plots for the confidence level between the Γ index and the equivalent N_{H} for the three observations.

None of the observations of this object presents a statistically significant iron line, although both a neutral iron line with the energy fixed to 6.4 keV and an iron line with the energy left free to vary were tested. During the eight days which the observations span, moderate flux variability between the first two observations and the last one was detected. Neither power-law index nor intrinsic absorption variation was measured. Figure 14 summarizes the results for the X-ray analysis of SDSS J162953.88+242638.3: the best-fit model for the three spectra with the residuals to the data, and the contour plots for the confidence level between the Γ index and the equivalent N_{H} for the three observations.

REFERENCES

- Baldwin, J. A., Phillips, M. M., & Terlevich, R. 1981, *PASP*, **93**, 5
- Benítez, E., Méndez-Abreu, J., Fuentes-Carrera, I., et al. 2012, arXiv:1212.1189
- Bian, W.-H., Chen, Y.-M., Gu, Q.-S., & Wang, J.-M. 2007, *ApJ*, **668**, 721
- Cardelli, J. A., Clayton, G. C., & Mathis, J. S. 1989, *ApJ*, **345**, 245
- Cid Fernandes, R., Mateus, A., Sodré, L., Stasińska, G., & Gomes, J. M. 2005, *MNRAS*, **358**, 363
- Cid Fernandes, R., Stasińska, G., Mateus, A., & Vale Asari, N. 2011, *MNRAS*, **413**, 1687
- Comerford, J. M., Griffith, R. L., Gerke, B. F., et al. 2009, *ApJL*, **702**, 82
- Coziol, R., Torres-Papaqui, J. P., Plauchu-Frayn, I., et al. 2011, *RMxAA*, **47**, 361
- Ferrarese, L., & Merritt, D. 2000, *ApJL*, **539**, 9
- Francis, P. J., Hewett, P. C., Foltz, C. B., et al. 1991, *ApJ*, **373**, 465
- Fu, H., Myers, A. D., Djorgovski, S. G., & Yan, L. 2011, *ApJ*, **733**, 103
- Fu, H., Yan, L., Myers, A. D., et al. 2012, *ApJ*, **745**, 67
- Gabriel, C., Denby, M., Fyfe, D. J., et al. 2004, in ASP Conf. Ser. 314, Astronomical Data Analysis Software and Systems (ADASS) XIII, ed. F. Ochsenbein, M. G. Allen, & D. Egret (San Francisco, CA: ASP), 759
- Gebhardt, K., Bender, R., Bower, G., et al. 2000, *ApJL*, **539**, 13
- Goodrich, R. W. 1989, *ApJ*, **340**, 190
- Goodrich, R. W. 1990, *ApJ*, **355**, 88
- Goodrich, R. W. 1995, *ApJ*, **440**, 141
- Ho, L. C. W. (ed.) 2004, *Coevolution of Black Holes and Galaxies* (Cambridge: Cambridge Univ. Press), 292
- Hu, J. 2008, *MNRAS*, **386**, 2242
- Kaspi, S., Maoz, D., Netzer, H., et al. 2005, *ApJ*, **629**, 61
- Kaspi, S., Smith, P. S., Netzer, H., et al. 2000, *ApJ*, **533**, 631
- Kauffmann, G., Heckman, T. M., Tremonti, C., et al. 2003, *MNRAS*, **346**, 1055
- Kewley, L. J., Dopita, M. A., Sutherland, R. S., Heisler, C. A., & Trevena, J. 2001, *ApJ*, **556**, 121
- Kewley, L. J., Groves, B., Kauffmann, G., & Heckman, T. 2006, *MNRAS*, **372**, 961
- Khachikian, E. Y., & Weedman, D. W. 1974, *ApJ*, **192**, 581
- Kormendy, J., Bender, R., & Cornell, M. E. 2011, *Natur*, **469**, 374
- Lampton, M., Margon, B., & Bowyer, S. 1976, *ApJ*, **208**, 177
- León-Tavares, J., Valtaoja, E., Chavushyan, V. H., et al. 2011, *MNRAS*, **411**, 1127
- Liu, X., Shen, Y., Strauss, M. A., & Greene, J. E. 2010, *ApJ*, **708**, 427
- Mateus, A., Sodré, L., Cid Fernandes, R., et al. 2006, *MNRAS*, **370**, 721
- Mazzarella, J. M., & Balzano, V. A. 1986, *ApJS*, **62**, 751
- McGurk, R. C., Max, C. E., Rosario, D. J., et al. 2011, *ApJL*, **738**, 2
- Mezcua, M., Lobanov, A. P., Chavushyan, V. H., & León-Tavares, J. 2011, *A&A*, **527**, A38
- Osterbrock, D. E. 1981, *ApJ*, **249**, 462
- Osterbrock, D. E., & Pogge, R. W. 1985, *ApJ*, **297**, 166
- Piconcelli, E., Jimenez-Bailón, E., Guainazzi, M., et al. 2004, *MNRAS*, **351**, 161
- Piconcelli, E., Jimenez-Bailón, E., Guainazzi, M., et al. 2005, *A&A*, **432**, 15
- Popović, L. Č., & Mediavilla, E. 1997, *POBeo*, **57**, 95
- Quillen, A. C., Shaked, S., Alonso-Herrero, A., et al. 2000, *ApJL*, **532**, 17
- Rafanelli, P., D'Abusco, R., Ciroi, S., et al. 2009, *NewAR*, **53**, 186
- Rafanelli, P., Marziani, P., Birkle, K., & Thiele, U. 1993, *A&A*, **275**, 451
- Rosario, D. J., Shields, G. A., Taylor, G. B., Salvander, S., & Smith, K. L. 2010, *ApJ*, **716**, 131
- Schlegel, D. J., Finkbeiner, D. P., & Davis, M. 1998, *ApJ*, **500**, 525
- Shen, J., Vanden Berk, D. E., Schneider, D. P., & Hall, P. B. 2008, *AJ*, **135**, 928
- Shen, Y., Liu, X., Greene, J. E., & Strauss, M. A. 2011, *ApJ*, **735**, 48
- Smith, K. L., Shields, G. A., Bonning, E. W., et al. 2010, *ApJ*, **716**, 866
- Stasińska, G., Cid Fernandes, R., Mateus, A., Sodré, L., & Asari, N. V. 2006, *MNRAS*, **371**, 972
- Tadhunter, C. 2008, *NewAR*, **52**, 227
- Torrealba, J., Benítez, E., Franco-Balderas, A., & Chavushyan, V. H. 2006, *RMxAA*, **42**, 3
- Trippie, M. L., Crenshaw, D. M., Deo, R. P., et al. 2010, *ApJ*, **725**, 1749
- Urry, C. M., & Padovani, P. 1995, *PASP*, **107**, 803
- Véron-Cetty, M., & Véron, P. 2010, *A&A*, **518**, A10
- Vestergaard, M. 2002, *ApJ*, **571**, 733
- Vestergaard, M., & Peterson, B. M. 2006, *ApJ*, **641**, 689
- Wandel, A., Peterson, B. M., & Malkan, M. A. 1999, *ApJ*, **526**, 579
- Wang, J.-M., Chen, Y.-M., Hu, C., et al. 2009, *ApJL*, **705**, 76
- Whittle, M. 1992, *ApJS*, **79**, 49
- Xanthopoulos, E. 1996, *MNRAS*, **280**, 6
- Xu, D., & Komossa, S. 2009, *ApJL*, **705**, 20
- York, D. G., Adelman, J., Anderson, J. E., Jr., et al. 2000, *AJ*, **120**, 1579